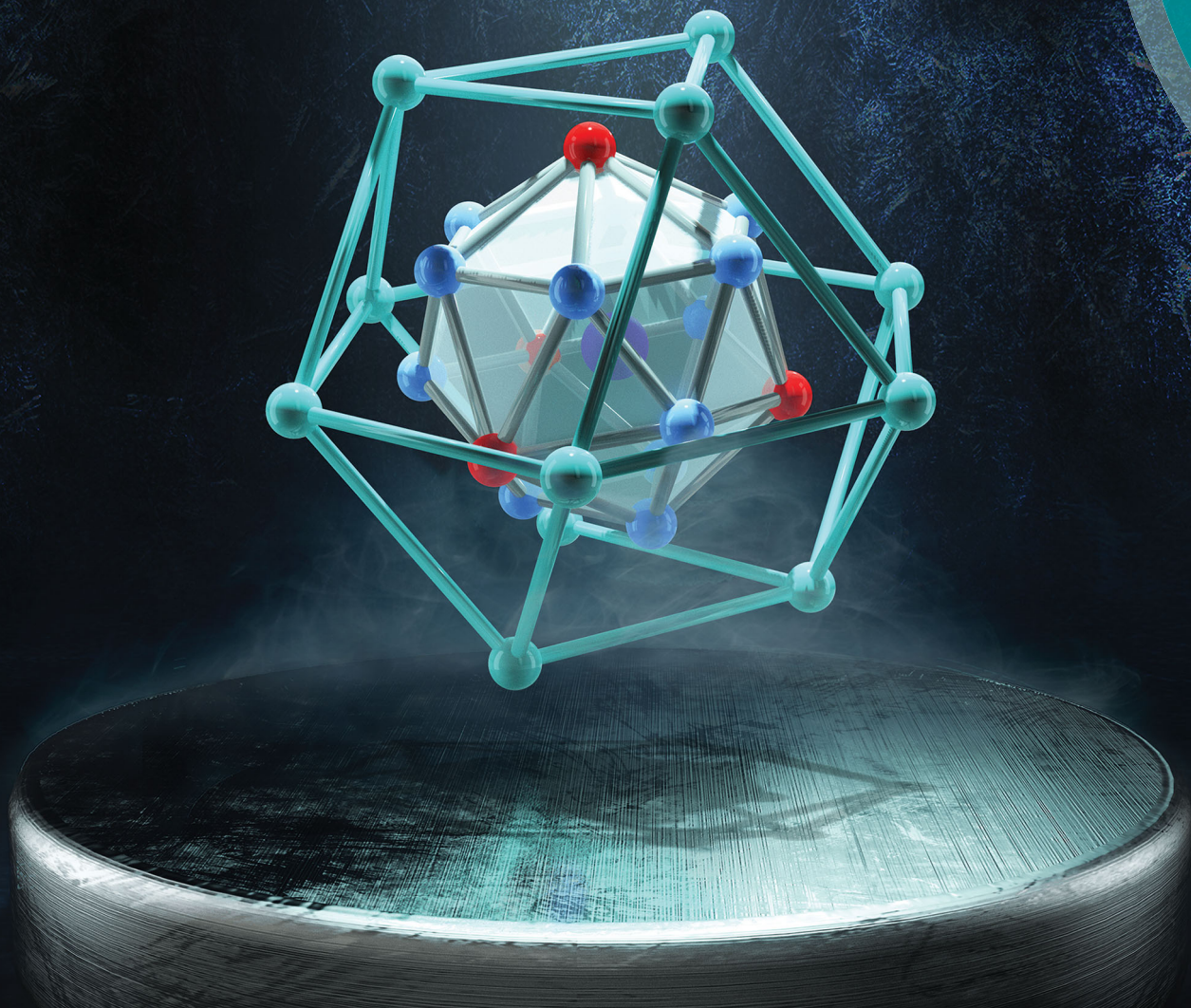


Journal of Materials Chemistry C

Materials for optical, magnetic and electronic devices

rsc.li/materials-c



ISSN 2050-7526



PAPER

Karoline Stolze *et al.*

High-entropy alloy superconductors on an α -Mn lattice



Cite this: *J. Mater. Chem. C*, 2018, 6, 10441

Received 6th July 2018,
Accepted 9th August 2018

DOI: 10.1039/c8tc03337d

rsc.li/materials-c

High-entropy alloy superconductors on an α -Mn lattice†

Karoline Stolze,  * F. Alex Cevallos, Tai Kong and Robert J. Cava

Previously unreported High-Entropy Alloys (HEAs) in the pentanary $(\text{ZrNb})_{1-x}[\text{MoReRu}]_x$, $(\text{HfTaWIr})_{1-x}[\text{Re}]_x$, and $(\text{HfTaWPt})_{1-x}[\text{Re}]_x$ systems are described and characterized. The materials have body-centered cubic α -Mn-type structures and mixed site occupancies; a small stoichiometry range is observed for all, and the mixed 4d–5d system has less Re than is typically encountered for Re-containing materials with this structure type. The latter two systems are the first reported 5d-element-only superconducting HEAs. All are type-II bulk superconductors with strongly varying critical temperatures (T_c s) depending on the cubic lattice parameter a and the valence electron count (VEC); the T_c s increase linearly with decreasing a and increasing VEC within each series and fall between the trend lines found for crystalline and amorphous transition metal alloy superconductors.

Introduction

Rapidly developing technologies require the parallel development of advanced materials with improved properties. Conventional metal alloys, for example, cannot fulfill all the demands of such technologies, motivating material scientists to continuously develop new materials. One new class of materials with an attractive combination of tunable mechanical and physical properties are the High-Entropy Alloys (HEAs).^{1–5} HEAs are multi-component materials composed of five or more elements combined in an equimolar or near-equimolar ratio. HEAs crystallize mainly in simple structures, such as face- or body-centered cubic (FCC, BCC) or hexagonal-closed packed (HCP) lattices with mixed site occupancy.^{6–8} In these solid-solutions, the high mixing entropy contributes significantly to the free energy, stabilizing the HEA phases at ambient temperatures.^{6,9,10,11}

HEAs have attracted much interest in recent years. Among the many studied systems only four examples of superconducting HEAs have so far been reported. The first, Ta–Nb–Hf–Zr–Ti,^{12–14} is a type-II bulk superconductor with a small unit cell BCC structure, a maximum $T_c \approx 7.6$ K for the composition $[\text{TaNb}]_{0.67}(\text{HfZrTi})_{0.33}$, an upper critical field for the quenching of superconductivity $\mu_0 H_{c2}$ at zero temperature of 7.75 Tesla (T), and extraordinarily robust zero-resistance superconductivity at pressures up to 190 GPa.¹⁵ In the next group, the CsCl structure is found, for pentanary $(\text{ScZrNb})_{1-x}[\text{RhPd}]_x$, and hexanary $(\text{ScZrNbTa})_{1-x}[\text{RhPd}]_x$ with a maximum $T_c \approx 9.3$ K and $\mu_0 H_{c2}(0) = 10.7$ T.¹⁶ These HEA

superconductor systems display strong composition-dependent changes in the superconducting transition temperature. Finally, the nearly equimolar BCC HEA $\text{Nb}_{21}\text{Re}_{16}\text{Zr}_{20}\text{Hf}_{23}\text{Ti}_{20}$ with $T_c \approx 5.3$ K and $\mu_0 H_{c2}(0) = 8.88$ T has been reported.¹⁷ Apparently, highly disordered BCC structures and their ordered variants with CsCl-type lattices, with small unit cells, seem to favor superconductivity in HEAs.

A rare, relatively complex structure type that is found for some superconducting binary alloys is the α -Mn structure. This structure derives from the low-temperature allotrope of manganese and is body-centered cubic with a relatively large crystallographic cell that contains many more atoms than the simple BCC and CsCl-type structures found for previously reported superconducting HEAs. These binary superconductors, in space group $I\bar{4}3m$ have 58 atoms per unit cell (rather than the two atoms per cell found in simple BCC materials) occupying four different symmetry sites, each of them with high coordination numbers.¹⁸ Typical elements forming binary α -Mn compounds with the general sum formula A_5B_{24} (two A_5B_{24} formula units per cell) are A: transition metal element or a rare earth element, and B: Mn, Tc, Re or Os. For these binaries, intermetallic compounds as well as solid solutions are reported. Although overall more complex than the small-cell BCC or FCC structures typically encountered for HEAs, the α -Mn structure type is also based on closest packing of atoms, though local closest packing rather than global closest packing dominates.¹⁹ Table 1 gives an overview of the conventional rhenium-based binary intermetallic α -Mn structure superconductors with $T_c > 2$ K listed in order of increasing VEC.^{20,21}

Here we present three previously unreported pentanary HEA superconductors with rhenium. They are in the mixed 4d 5d system Zr–Nb–Mo–Re–Ru, and in the purely 5d systems

Department of Chemistry, Princeton University, Princeton, New Jersey 08544, USA.
E-mail: kstolze@princeton.edu

† Electronic supplementary information (ESI) available. See DOI: 10.1039/c8tc03337d

Table 1 Rhenium based binary intermetallic and alloy superconductors with α -Mn structure, $T_c > 2$ K^{20,21}

Compound	T_c (K)	VEC (e per atom)
ScRe ₃	2.2	6.00
AlRe ₃	3.4	6.00
HfRe ₃	5.9	6.25
Ti ₅ Re ₂₄	6.6	6.48
TaRe ₃	6.8	6.50
Zr _{0.14} Re _{0.86}	7.4	6.58
Nb _{0.18} Re _{0.82}	8.9	6.64
WRe ₃	9.0	6.75
MoRe ₃	9.9	6.75

Hf-Ta-W-Re-Ir and Hf-Ta-W-Re-Pt. These latter systems are the first HEA superconductors based solely on 5d-elements and therefore may be of great interest due to their spin-orbit coupling.^{22–24} The materials have the α -Mn structure with mixed site occupancy and reveal strongly composition-dependent superconducting transition temperatures.

Experimental

Synthesis

All samples were prepared by mixing stoichiometric amounts of zirconium foil (99.8% purity), niobium pieces (99.99% purity), tantalum (99.9% purity, arc-melted from powder), molybdenum foil (99.95% purity), ruthenium pieces (99.9% purity, arc-melted from powder), hafnium pieces (99.6% purity, arc-melted from powder), tantalum foil (99.9% purity), tungsten foil (99.95% purity), rhenium pieces (99.99% purity), and platinum pieces (99.99% purity, arc-melted from powder) respectively, all from Alfa Aesar. The elemental metals were carefully arc melted in 200 or 250 mg sample sizes into a single metallic button under an argon atmosphere with a high current ($T > 2500$ °C, $I < 75$ A) and quenched on a water-chilled copper plate. The argon atmosphere was cleaned of residual oxygen and moisture by co-heating of a zirconium sponge at each melting step. The samples were re-melted at least three times and turned over each time, to ensure the optimal mixing of the constituents. Only samples with a weight loss less than 1.5% were characterized. An overview of the samples studied, with the normalized sum formulas, corresponding molar composition, total weight loss from starting weight during preparation, lattice parameter a of the α -Mn structure, and valence electron concentrations (VECs, *i.e.* electrons per atom, e/a) is given in Table 2. VECs only for single-phase samples are shown in the table. No amorphous phases are present in the HEA samples, because for such metallic systems cooling rates of several orders of magnitude faster than those employed here would be required to obtain an amorphous phase.

Crystallography

For qualitative structural characterization, powder X-ray diffractometry (pXRD) was used. All samples are brittle and were converted into powder form by grinding. The pXRD patterns were obtained on a Bruker D8 Advance Eco in Bragg-Bretano Geometry with Cu-K α -radiation and a LynxEye-XE detector.

LeBail fits for determining the average cell parameters of all samples were performed using the TOPAS program package²⁵ with Thompson-Cox-Hastings pseudo-Voigt peak shapes.

Physical property measurements

The magnetizations, resistivities and heat capacities were studied on bulk sample pieces using a Quantum Design Physical Property Measurement System (PPMS) DynaCool equipped with a Vibrating Sample Magnetometer (VSM) Option. Zero-field cooled (ZFC) temperature dependent magnetization measurements were carried in a field of $\mu_0H = 2$ mT. For the resistivity measurements, a standard four-probe technique was used with an applied current of $I = 3$ mA. The specific heat experiments were carried out using a relaxation method in the temperature interval of 15–1.8 K at zero applied magnetic field and 9 T.

Electron microscopy

Compositions were verified for selected materials by performing energy dispersive X-ray spectroscopy (EDX) studies on flat sanded sample surfaces with the accelerating voltage of 15 kV with a Quanta 200 FEG Environmental (FEI) scanning electron microscope equipped with a X-Max 80 mm² SDD (Oxford Instruments) spectrometer, collected and analyzed employing the INCA suite of programs.

Results and discussion

Structural characterization of α -Mn type HEAs

$(\text{ZrNb})_{1-x}[\text{MoReRu}]_x$. The high-temperature reaction of the 4d transition metals zirconium, niobium, molybdenum and ruthenium together with the 5d-metal rhenium with the general sum formula $(\text{ZrNb})_{1-x}[\text{MoReRu}]_x$ forms, for $0.90 \leq x \leq 0.70$, brittle, silver-lustrous, polycrystalline materials that are stable in air and moisture. The brittle character of these and the other α -Mn type HEAs studied in this work is in stark contrast to the ductile character of the small-cell superconducting BCC and CsCl-type HEAs studied previously. Their pXRD patterns could be indexed with the complex structure of the low-temperature allotrope of manganese, *i.e.* α -Mn.¹⁸ The compounds crystallize on a body-centered cubic lattice in space group $I\bar{4}3m$ (Fig. 1) whose unit cell contains 58 atoms occupying four different Wyckoff sites: $2a$ (0,0,0), $8c$ (x,x,x), and $2 \times 24g$ (x,x,z). The coordination spheres of the atoms in each site reveal high coordination numbers (CN) and can be described as distorted 4-fold capped truncated tetrahedra representing so called Friauf-polyhedra with CN = 16 for sites $2a$ (less distorted) and $8c$ (more distorted), a polyhedron with CN = 13 whose faces are 19 triangles and one trapezoid for one $24g$ site, and a distorted icosahedron for the other $24g$ site (CN = 12), all depicted in Fig. 2.¹⁸ The α -Mn structure is built up by the interpenetration of those four different coordination polyhedra, determined by local closest packing of the vertices. Another way to describe the structure is with polyhedral nesting: the atom on $2a$ (center and the corner of the unit cell) is coordinated by twelve atoms located on $24g$ forming a truncated tetrahedron with four

Table 2 Sample overview for the α -Mn-type HEAs studied with sum formula, corresponding composition, total mass loss during sample preparation, lattice parameter a of the α -Mn structure in $I\bar{4}3m$, and VEC of phase-pure α -Mn type samples

Normalized sum formula	x	Composition	Δm^a (%)	a (Å), ± 0.001	VEC (e/a) ^b
(ZrNb) _{0.30} [MoReRu] _{0.60}	0.60	Zr _{0.20} Nb _{0.20} Mo _{0.2333} Re _{0.20} Ru _{0.20}	0.32		
(ZrNb) _{0.30} [MoReRu] _{0.70}	0.70	Zr _{0.15} Nb _{0.15} Mo _{0.2333} Re _{0.2333} Ru _{0.2333}	0.32	9.775	
(ZrNb) _{0.20} [MoReRu] _{0.80}	0.80	Zr _{0.10} Nb _{0.10} Mo _{0.2667} Re _{0.2667} Ru _{0.2667}	0.32	9.701	6.50
(ZrNb) _{0.10} [MoReRu] _{0.90}	0.90	Zr _{0.05} Nb _{0.05} Mo _{0.30} Re _{0.30} Ru _{0.30} ^c	1.00	9.613	6.75
(ZrNb) _{0.00} [MoReRu] _{1.00}	1.00	Mo _{0.3333} Re _{0.3333} Ru _{0.3333}	0.18		
(HfTaWIr) _{1.00} [Re] _{0.00}	0.00	Hf _{0.25} Ta _{0.25} W _{0.25} Ir _{0.25}	0.30		
(HfTaWIr) _{0.90} [Re] _{0.10}	0.10	Hf _{0.225} Ta _{0.225} W _{0.225} Ir _{0.225} Re _{0.10}	0.25		
(HfTaWIr) _{0.80} [Re] _{0.20}	0.20	Hf _{0.20} Ta _{0.20} W _{0.20} Ir _{0.20} Re _{0.20}	0.67	9.899	
(HfTaWIr) _{0.70} [Re] _{0.30}	0.30	Hf _{0.175} Ta _{0.175} W _{0.15} Ir _{0.175} Re _{0.30}	1.05	9.820	
(HfTaWIr) _{0.60} [Re] _{0.40}	0.40	Hf _{0.15} Ta _{0.15} W _{0.15} Ir _{0.15} Re _{0.40}	0.85	9.778	
(HfTaWIr) _{0.50} [Re] _{0.50}	0.50	Hf _{0.125} Ta _{0.125} W _{0.125} Ir _{0.125} Re _{0.50}	0.60	9.741	
(HfTaWIr) _{0.45} [Re] _{0.55}	0.55	Hf _{0.1125} Ta _{0.1125} W _{0.1125} Ir _{0.1125} Re _{0.55}	0.90	9.734	
(HfTaWIr) _{0.40} [Re] _{0.60}	0.60	Hf _{0.10} Ta _{0.10} W _{0.10} Ir _{0.10} Re _{0.60}	0.60	9.723	6.60
(HfTaWIr) _{0.35} [Re] _{0.65}	0.65	Hf _{0.0875} Ta _{0.0875} W _{0.0875} Ir _{0.0875} Re _{0.65}	1.00	9.701	6.65
(HfTaWIr) _{0.30} [Re] _{0.70}	0.70	Hf _{0.075} Ta _{0.075} W _{0.075} Ir _{0.075} Re _{0.70}	0.90	9.662	6.70
(HfTaWIr) _{0.25} [Re] _{0.75}	0.75	Hf _{0.0625} Ta _{0.0625} W _{0.0625} Ir _{0.0625} Re _{0.75}	0.95	9.642	6.75
(HfTaWIr) _{0.20} [Re] _{0.80}	0.80	Hf _{0.05} Ta _{0.05} W _{0.05} Ir _{0.05} Re _{0.80}	0.60	9.638	
(HfTaWPt) _{0.60} [Re] _{0.40}	0.40	Hf _{0.15} Ta _{0.15} W _{0.15} Pt _{0.15} Re _{0.40}	0.81	9.767	
(HfTaWPt) _{0.50} [Re] _{0.50}	0.50	Hf _{0.125} Ta _{0.125} W _{0.125} Pt _{0.125} Re _{0.50}	0.65	9.726	
(HfTaWPt) _{0.45} [Re] _{0.55}	0.55	Hf _{0.1125} Ta _{0.1125} W _{0.1125} Pt _{0.1125} Re _{0.55}	0.44	9.701	
(HfTaWPt) _{0.40} [Re] _{0.60}	0.60	Hf _{0.10} Ta _{0.10} W _{0.10} Pt _{0.10} Re _{0.60}	0.76	9.683	6.70
(HfTaWPt) _{0.35} [Re] _{0.65}	0.65	Hf _{0.0875} Ta _{0.0875} W _{0.0875} Pt _{0.0875} Re _{0.65}	1.32	9.667	6.74
(HfTaWPt) _{0.30} [Re] _{0.70}	0.70	Hf _{0.075} Ta _{0.075} W _{0.075} Pt _{0.075} Re _{0.70}	0.90	9.648	6.78
(HfTaWPt) _{0.25} [Re] _{0.75}	0.75	Hf _{0.0625} Ta _{0.0625} W _{0.0625} Pt _{0.0625} Re _{0.75}	0.76	9.636	
(HfTaWPt) _{0.20} [Re] _{0.80}	0.80	Hf _{0.05} Ta _{0.05} W _{0.05} Pt _{0.05} Re _{0.80}	0.25	9.635	

^a Total weight measured to 1 part in 2500 or 1 part in 2000; error from measured weight loss is $\leq 1.0\%$ in the 4d/5d-element family and $< 1.4\%$ in the 5d-element families. There is no indication of preferential element loss for these materials and therefore the errors in column six have been estimated if the weight loss is equal for all elements present. ^b e/a = electrons per atom. Maximum error is ± 0.03 e/a for Δm originating equally from all elements present. ^c Elemental analysis: expected (at%) 5.0, 5.0, 30.0, 30.0, 30.0 for Zr, Nb, Mo, Re and Ru, observed by EDX (estimated error $\pm 2\%$) 4.8, 4.8, 30.1, 29.9, 30.4. ^d Elemental analysis: expected (at%) 10.0, 10.0, 10.0, 10.0, 60.0 for Hf, Ta, W, Ir and Re, observed by EDX (estimated error $\pm 2\%$) 10.6, 8.5, 8.1, 9.9, 63.0. ^e Elemental analysis: expected (at%) 10.0, 10.0, 10.0, 10.0, 60.0 for Hf, Ta, W, Pt and Re, observed by EDX (estimated error $\pm 2\%$) 9.0, 8.0, 8.3, 8.3, 66.5.

triangular and four hexagonal faces. The hexagonal faces are capped by four atoms sitting on $8c$ in a tetrahedral fashion around the central atom. The last coordination sphere is built up by the twelve atoms sitting on the second $24g$ site forming a cuboctahedron.¹⁹ Within both structural principles, local dense packing of atoms stabilizes the α -Mn structure type in the studied HEA systems. The binary intermetallic structures determined in this structure type generally have a well-defined A_5B_{24} (*i.e.* $A_{0.17}B_{0.83}$) stoichiometry with ordering of the two different atom types; atom A found on Wyckoff sites $2a$ and $8c$, and atom B on the two $24g$ sites.²⁶ The solid solutions are non-stoichiometric A_xB_{1-x} compounds with either partial ordering on certain sites, *e.g.* as in $Re_{0.6}Nb_{0.4}$ ²⁷ and $Re_{0.8}Nb_{0.2}$,²⁸ or complete random mixing of the two elements on all four symmetry sites, as reported *e.g.* for $Re_{0.67}Ta_{0.33}$.²⁸ All binary α -Mn-structure superconducting alloys based on Re are Re-rich – that is, they contain more than 50% Re and often much more; which is not the case for the HEA superconductors studied here.

We find that phase-pure α -Mn type $(ZrNb)_{1-x}[MoReRu]_x$ HEAs form with $0.90 \leq x \leq 0.80$ (Fig. 2, grey shaded pXRD patterns), indicating a small but distinct phase width of the structure type that shows the compounds ability to form a solid solution with certain mixing of the different metals on the different sites. The large numbers of different atoms and the large number of sites in this crystal structure means that an unambiguous determination of the atomic site occupancies of

our superconducting α -Mn HEAs is beyond the scope of the present study, as it would require the co-refinement of several sets of diffraction data designed such that the atoms have different scattering factors. Just like the recently reported CsCl-type HEAs,¹⁶ the new α -Mn HEAs are materials partway between ordered intermetallic compounds and random solid solution, and appear to be stabilized within a small compositional range due to a delicate balance between maximizing the mixing entropy and minimizing the mixing enthalpy.

The phase boundary of α -Mn type $(ZrNb)_{1-x}[MoReRu]_x$ HEAs for high x values is an HCP alloy of equimolar MoReRu with mixed site occupancy (Fig. 1). This material is superconducting at $T_c \approx 9.1$ K. For low x values, *i.e.* $x \leq 0.70$, two BCC phases with slightly different lattice parameters [$a_1 = 3.176(1)$ Å, $a_2 = 3.211(1)$ Å] are found in addition to the α -Mn-type HEA alloy, and, with further increase of the Zr/Nb content the target compound is not formed any more but the hexagonal Laves phase $ZrRe_2$ [$P6_3/mmc$, $a = 5.261(1)$ Å, $c = 8.593(1)$ Å] appears. Thus, the HEA with the α -Mn structure forms for compositions between those of intermetallic alloys with fewer metal constituents, *i.e.* alloys with lower mixing entropy.

(HfTaWIr)_{1-x}[Re]_x and (HfTaWPt)_{1-x}[Re]_x. The combination of exclusively 5d transition metal elements with the compositions $(HfTaWIr)_{1-x}[Re]_x$ and $(HfTaWPt)_{1-x}[Re]_x$ gave samples with the α -Mn-type lattice ($I\bar{4}3m$), (Fig. 3). Phase-pure α -Mn-type HEAs could be obtained for these systems for $0.75 \leq x \leq 0.60$

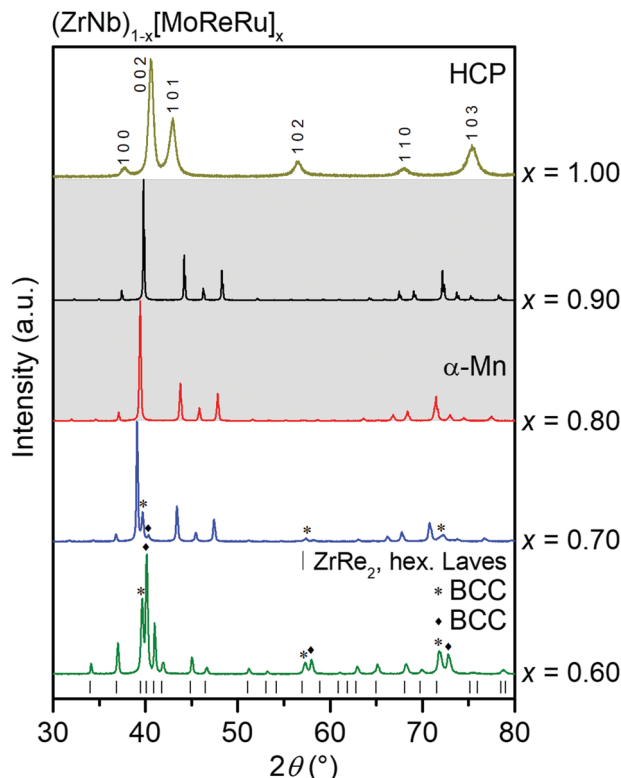


Fig. 1 PXRD patterns of powder samples of $(\text{ZrNb})_{1-x}[\text{MoReRu}]_x$ with $x = 1.00\text{--}0.60$. The different symbols mark the peak position for the reflections of emerging phases for high and low x ; HCP solid solution of MoReRu for high $x = 1.00$, and two BCC phases and the hexagonal Laves phase ZrRe_2 ($P6_3/mmc$) for low x values. All unmarked peaks belong to the $\alpha\text{-Mn}$ -type lattice ($\bar{I}\bar{4}3m$); the grey shaded patterns are phase-pure $\alpha\text{-Mn}$ -type samples.

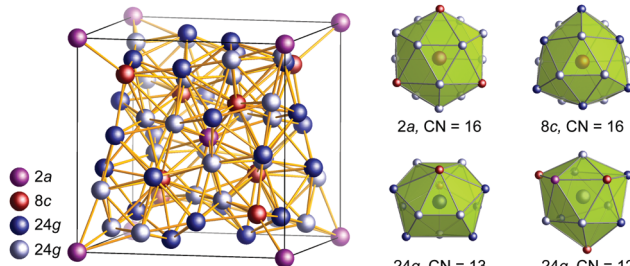


Fig. 2 Left: Unit cell of body-centred cubic $\alpha\text{-Mn}$ structure ($\bar{I}\bar{4}3m$) with four different Wyckoff sites; right: representation of the coordination polyhedra for each symmetry site with high CN each.

and $0.70 \leq x \leq 0.60$, respectively (Fig. 3, grey shaded PXRD patterns). The lattice parameter a varies depending on the material's composition and stoichiometry, *i.e.* between $9.638(1)$ Å $\leq a \leq 9.869(1)$ Å for the Ir-variant and $9.635(1)$ Å $\leq a \leq 9.767(1)$ Å for the Pt-variant (Table 2). Again, the distinct phase width of the structure type shows that the compounds form a solid solution with certain mixing of the different metals on the sites within the structure. Whether the rhenium atoms prefer to exclusively occupy both the low symmetry $24g$ positions, *e.g.* as in $\text{Hf}_5\text{Re}_{24}$,²⁶ and the other four transition metals

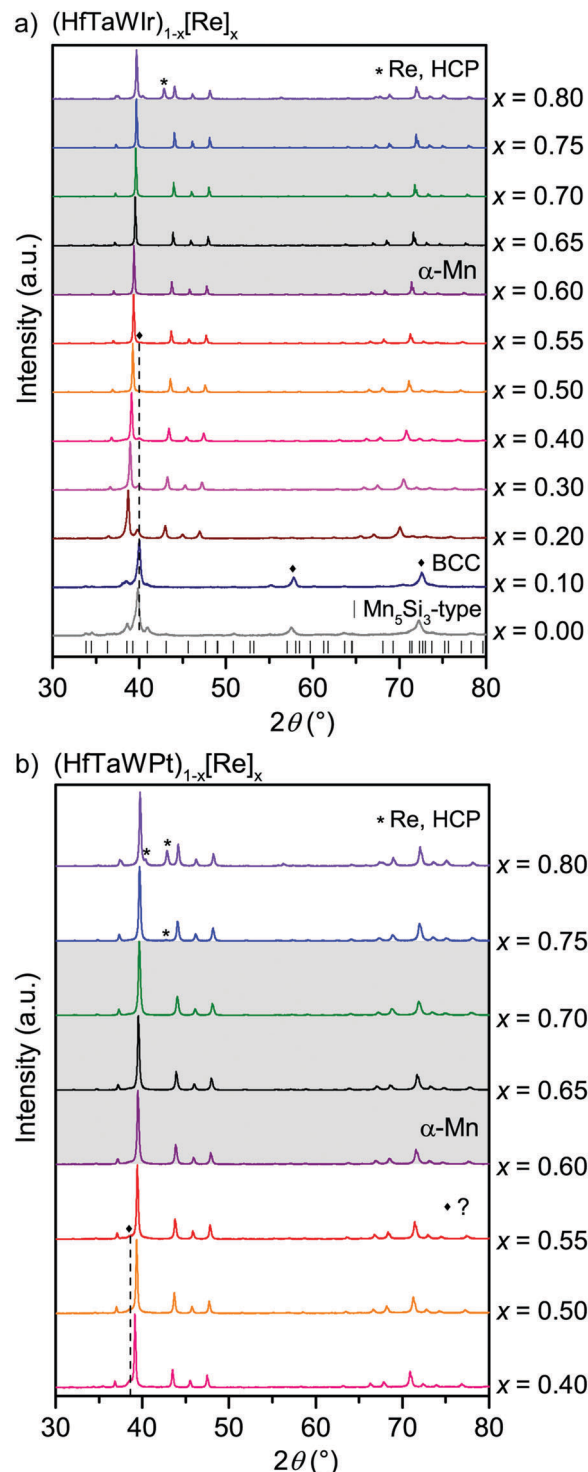


Fig. 3 PXRD patterns of powder samples of (a) $(\text{HfTaWIr})_{1-x}[\text{Re}]_x$ with $x = 0.80\text{--}0.00$ and (b) $(\text{HfTaWPt})_{1-x}[\text{Re}]_x$ with $x = 0.80\text{--}0.40$. The different symbols mark the peak position for the reflections of emerging phases for high and low x respectively; HCP rhenium for high x , and (a) a BCC phase and a Mn_5Si_3 -type phase ($P6_3/mcm$) for low x values; and (b) one peak for an unknown minority phase. All unmarked peaks belong to the $\alpha\text{-Mn}$ -type lattice ($\bar{I}\bar{4}3m$); the grey shaded patterns are phase-pure $\alpha\text{-Mn}$ -type samples.

mix on Wyckoff sites $2a$ and $8c$ or whether all metals mix randomly on all four crystallographic positions in the structure,

cannot be determined unambiguously for a system with 5 elements present by employing only one type of diffraction. In both HEA systems, elemental rhodium starts to separate out for high x -values in addition to the target phase (Fig. 3a and b). On the other side, the phase boundary for the α -Mn type $(\text{HfTaWIr})_{1-x}[\text{Re}]_x$ phase at low x -values is a BCC phase [$a = 3.2020(1)$ Å], and with further decrease of the Re content a Mn_3Si_3 -type phase [$P6_3/mcm$, $a = 7.942(1)$ Å, $c = 5.296(1)$ Å] appears (Fig. 3a). In these pure 5d-metal systems the HEAs are Re-rich.

The $(\text{HfTaWIr})_{1-x}[\text{Re}]_x$ compounds are stable in air and moisture. In contrast, the $(\text{HfTaWPt})_{1-x}[\text{Re}]_x$ samples start to decompose after approximately seven days in air, changing color from lustrous silver to black while emitting a dark colored liquid with $\text{pH} \approx 2$. Although the crystal structure of the bulk of the aged samples seems not to change according to pXRD measurements (no peak shift, no broadening, no splitting, no intensity loss), the examination of the microstructure and the chemical composition of the surface of a decomposed initially phase-pure α -Mn-type HEA $(\text{HfTaWPt})_{0.40}[\text{Re}]_{0.60}$, exemplary of the Pt-variant compounds, using SEM and EDX, revealed significant differences compared to an as-synthesized bulk sample of the same age (stored in the inert Ar-atmosphere of a glove box) of the same composition and crystal structure: the as-synthesized $(\text{HfTaWPt})_{0.40}[\text{Re}]_{0.60}$ sample shows the flat, smooth surface of a metallic nugget without a visible microstructure under our imaging conditions, homogeneous distribution of all five elements, and a stoichiometry in good agreement with the initial element composition [EDX: expected (at%) 10.0, 10.0, 10.0, 10.0, 60.0 for Hf, Ta, W, Pt and Re, observed (estimated error $\pm 2\%$) 9.0, 8.0, 8.3, 8.3, 66.5, Fig. S1, ESI[†]]. In contrast, the surface of the decomposed $(\text{HfTaWPt})_{0.40}[\text{Re}]_{0.60}$ material displays a remarkable, porous microstructure, reminiscent of de-alloying.^{29–31} It shows sub-micrometer dendrites that are significantly Hf/Pt-rich (EDX: Hf: 43.2 at% and Pt: 56.8 at%, Fig. S2, ESI[†]) that form on the surface of the remaining bulk alloy. The characterization of the slow decomposition of the superconducting $(\text{HfTaWIr})_{1-x}[\text{Re}]_x$ HEA material and the accumulation of a dendritic Hf/Pt-rich phase on its surface is beyond the scope of the current work and may be of interest for future studies.

Composition dependence of the superconducting transition temperature and heat capacity in the α -Mn type HEAs

The superconducting properties of the α -Mn type HEAs were generally characterized through zero-field cooled (ZFC) temperature-dependent magnetization measurements. The magnetization curves for the three α -Mn type HEA superconducting materials $(\text{ZrNb})_{1-x}[\text{MoReRu}]_x$, $(\text{HfTaWIr})_{1-x}[\text{Re}]_x$ and $(\text{HfTaWPt})_{1-x}[\text{Re}]_x$ for samples with different compositions were measured from 1.7 K to 8 K or 10 K (Fig. 4a–c). The susceptibility χ for all samples in the superconducting state, except for $(\text{HfTaWIr})_{0.7}[\text{Re}]_{0.3}$, whose superconducting transition is not complete above 1.7 K, is more negative than -1 , the ideal diamagnetic response for superconducting materials. This common phenomenon is caused by demagnetization effects. For a better comparison,

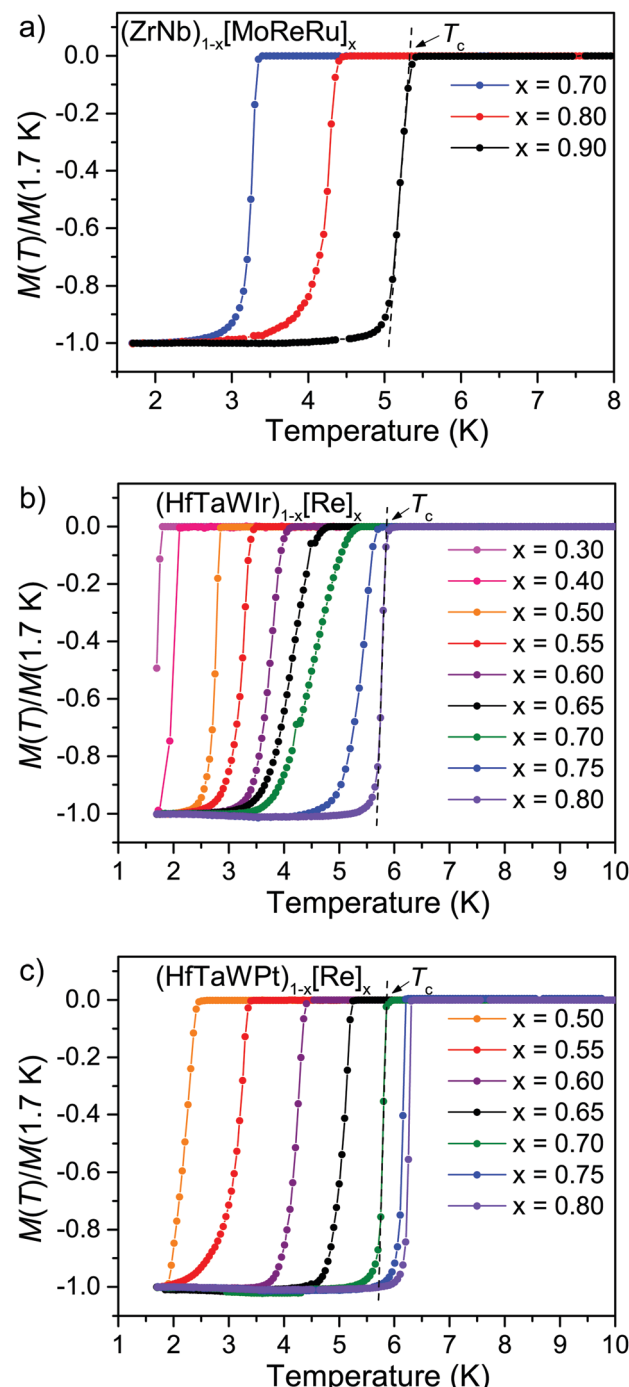


Fig. 4 Composition dependence of the superconducting transition in (a) $(\text{ZrNb})_{1-x}[\text{MoReRu}]_x$ with $x = 0.90–0.70$; (b) $(\text{HfTaWIr})_{1-x}[\text{Re}]_x$ with $x = 0.80–0.30$; (c) $(\text{HfTaWPt})_{1-x}[\text{Re}]_x$ with $x = 0.80–0.50$. Normalized temperature dependent ZFC magnetization, measured in an external magnetic field of $\mu_0 H = 2$ mT.

the magnetization curves are normalized by plotting the χ data as $M(T)/M(1.7 \text{ K})$. The values for the superconducting critical temperatures T_c were determined conservatively from the crossing of the linearly approximated diamagnetic slopes near the superconducting transition and the normal-state magnetizations (dashed black lines Fig. 4a–c). The superconducting

transitions in $\chi(T)$ for all investigated α -Mn type HEAs samples are well defined in temperature and exhibit a steep slope, except for $(\text{HfTaWIr})_{0.30}[\text{Re}]_{0.70}$ (Fig. 4b, green curve), whose transition is broad; this breadth can be explained as due to small chemical inhomogeneities in this sample.

The temperature-dependent magnetization curves reveal a dramatic change of the T_c for small variations of the HEAs' composition. For all three HEA series, T_c increases with increasing x , which correlates with increasing Re-content and decreasing lattice constant a of the cubic α -Mn structure. The maximum transition temperatures can be found for $x = 0.90$, with $T_c = 5.3$ K in the $(\text{ZrNb})_{1-x}[\text{MoReRu}]_x$ series, for $x = 0.80$ with $T_c = 5.9$ K in the $(\text{HfTaWIr})_{1-x}[\text{Re}]_x$ series, and for $x = 0.80$ with $T_c = 6.3$ K in the $(\text{HfTaWPt})_{1-x}[\text{Re}]_x$ series. Although the latter two materials of the 5d-element HEA series are not phase-pure, as they have started to segregate out elemental rhenium (Fig. 3a and b; violet curves), the decrease of their lattice parameter a still indicates a systematic change of the materials composition near these limits (see Table 2). In addition, elemental Re is not superconducting.

The lattice-parameter-dependent change of the superconducting transition temperature $T_c(a)$ for the new α -Mn type $(\text{ZrNb})_{1-x}[\text{MoReRu}]_x$, $(\text{HfTaWIr})_{1-x}[\text{Re}]_x$ and $(\text{HfTaWPt})_{1-x}[\text{Re}]_x$ HEAs, shown in Fig. 5a, reveals a linear increase of the T_c with decreasing lattice constant for all these α -Mn type HEA materials. The $(\text{HfTaWPt})_{1-x}[\text{Re}]_x$ HEA shows the largest change of T_c as a function of the lattice parameter: while $(\text{HfTaWPt})_{0.50}[\text{Re}]_{0.50}$ for example is superconducting at around 2.4 K, a decrease of a by less than 1% causes a significant increase of the T_c up to ~ 6.3 K for $x = 0.8$. In addition, the valence electron count dependency of the superconducting transition temperatures of the phase-pure α -Mn type $(\text{ZrNb})_{1-x}[\text{MoReRu}]_x$, $(\text{HfTaWIr})_{1-x}[\text{Re}]_x$ and $(\text{HfTaWPt})_{1-x}[\text{Re}]_x$ HEA samples shows a monotonic and almost linear trend for all three systems (Fig. 5b, black squares, red triangles, blue circles). With increasing VEC the T_c increases. This kind of behavior falls in between the trend lines found for crystalline transition metals and their binary alloys and intermetallic compounds, known as the Matthias rule (Fig. 5b, dark blue trend line),³² and for amorphous transition metal alloy films, reported by Colver and Hammond (Fig. 5b, light blue trend line).³³ Compared to the benchmarks of Matthias, which show maxima near VECs of 5 and 7 e/a, and Colver and Hammond's trend line, which shows a monotonic increase of the superconducting transition temperature with increasing VEC, reaching a maximum around 6.4 e/a, the T_c vs. VEC behavior of the superconducting α -Mn type HEA series show intermediate slopes with maximum values around 6.75 e/a. These VEC values match those displayed by the compositions of the binary rhenium alloys with α -Mn type structure that exhibit the highest T_c s, i.e. MoRe_3 ($T_c = 9.9$ K) and WRe_3 ($T_c = 9.0$ K)¹³ (Table 1). In addition, the T_c vs. VEC trends of the α -Mn type HEAs match the one of their binary isostructural relatives (Fig. 5b, green trend line). It must be noted that the trend lines of all three α -Mn type HEA series do not reveal distinct maxima as a structural phase separation occurs for compositions with higher VECs. In contrast to the foregoing findings, the CsCl-type HEA superconductors $(\text{ScZrNb})_{1-x}[\text{RhPd}]_x$ and $(\text{ScZrNbTa})_{1-x}[\text{RhPd}]_x$

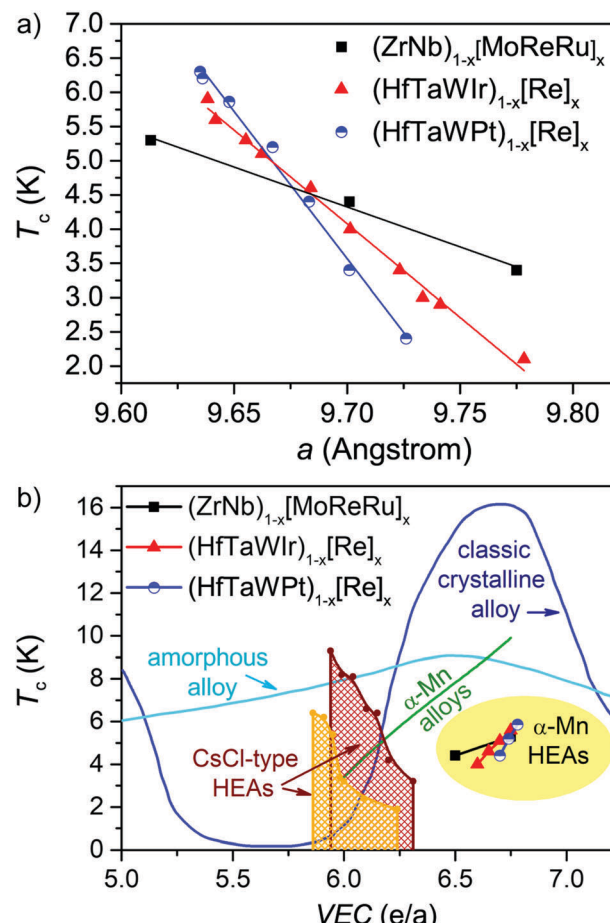


Fig. 5 (a) Lattice parameter a dependency of the superconducting transition temperatures of the α -Mn type $(\text{ZrNb})_{1-x}[\text{MoReRu}]_x$, $(\text{HfTaWIr})_{1-x}[\text{Re}]_x$ and $(\text{HfTaWPt})_{1-x}[\text{Re}]_x$ HEAs; the lines represent the linear fit of the data points. (b) Valence electron count dependency of the superconducting transition temperatures of phase-pure α -Mn type $(\text{ZrNb})_{1-x}[\text{MoReRu}]_x$, $(\text{HfTaWIr})_{1-x}[\text{Re}]_x$ and $(\text{HfTaWPt})_{1-x}[\text{Re}]_x$ samples (pale yellow shading) compared to the T_c vs. VEC trend lines of CsCl-type HEAs, binary α -Mn type alloys with rhenium, classic crystalline alloys, and amorphous alloy films.

show a maximum at the electron count of 5.9 e/a and follow a strict monotonically decreasing trend with increasing VEC (Fig. 5b, orange and dark red trend lines).¹⁶

The α -Mn type $(\text{ZrNb})_{1-x}[\text{MoReRu}]_x$, $(\text{HfTaWIr})_{1-x}[\text{Re}]_x$ and $(\text{HfTaWPt})_{1-x}[\text{Re}]_x$ HEA superconductors were also studied by measuring their heat capacity $C(T)$ in order to gain more information about the nature of the superconductivity. The temperature-dependent specific heat capacities C/T vs. T , measured without applied magnetic field in the vicinity of the superconducting transition of the phase-pure samples $(\text{ZrNb})_{0.10}[\text{MoReRu}]_{0.90}$, $(\text{HfTaWIr})_{0.40}[\text{Re}]_{0.60}$, and $(\text{HfTaWPt})_{0.40}[\text{Re}]_{0.60}$ are shown in Fig. 6a–c. All three HEAs reveal single well-defined transitions, which occur at 5.3 K, 4.0 K, and 4.4 K respectively. These temperatures are consistent with the results from the susceptibility measurements (compare Table S1, ESI†), and confirm the presence of a single superconducting phase. With the equal-area construction of the specific heat jump in C/T vs. T at T_c and the calculated value for γ (see Fig. S3, ESI†),

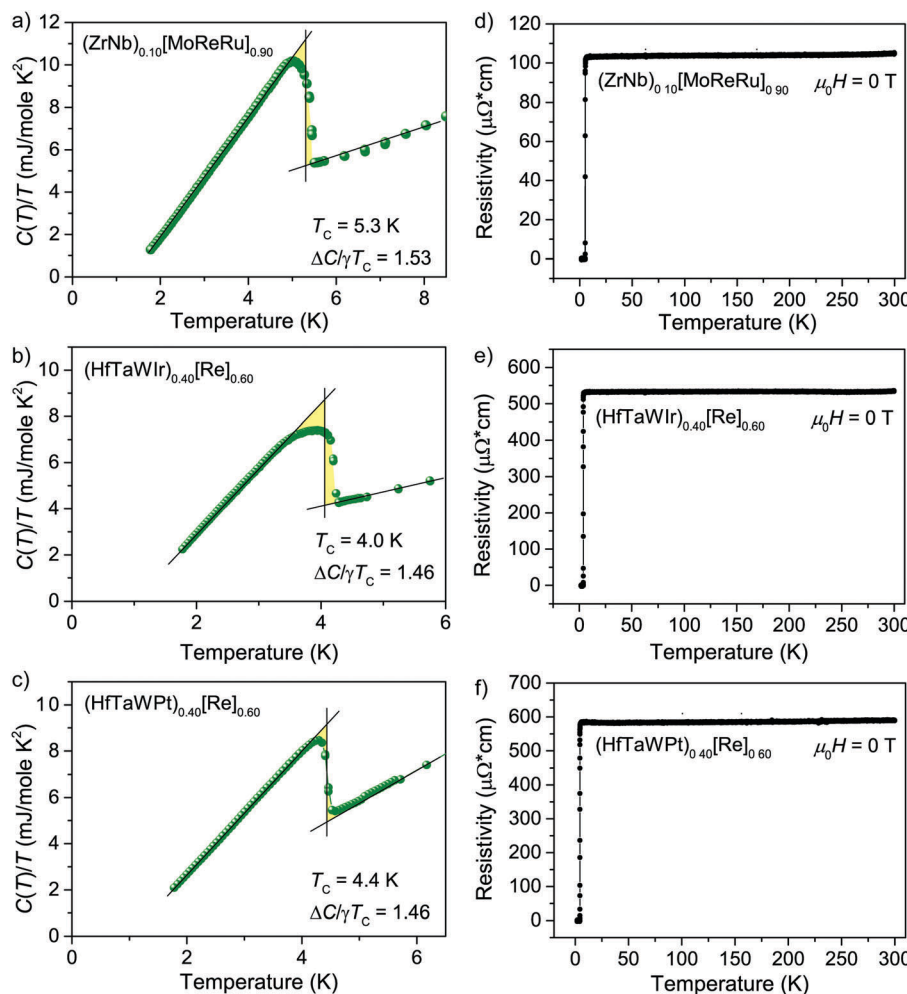


Fig. 6 C/T vs. T plot for (a) $(ZrNb)_{0.10}[MoReRu]_{0.90}$, (b) $(HfTaWIr)_{0.40}[Re]_{0.60}$, and (c) $(HfTaWPt)_{0.40}[Re]_{0.60}$ measured in zero applied magnetic field, the solid black lines emphasize the equal area construction (pale yellow shading) used for the estimation of T_c and the superconducting jump $\Delta C/\gamma T_c$. Temperature dependent electrical resistivity $\rho(T)$ of (d) $(ZrNb)_{0.10}[MoReRu]_{0.90}$, (e) $(HfTaWIr)_{0.40}[Re]_{0.60}$, and (f) $(HfTaWPt)_{0.40}[Re]_{0.60}$ with no applied magnetic field.

the $\Delta C/\gamma T_c$ ratios were obtained (Table S1, ESI[†]), and are very close to the standard weak-coupling BSC value, *i.e.* $\Delta C/\gamma T_c = 1.43$. Thus, all three α -Mn HEAs are bulk superconductors that exhibit weak-coupling superconductivity. For more details we refer readers to the ESI.[†]

Resistivity and upper critical fields of the α -Mn type HEAs

The temperature-dependent electrical resistivity $\rho(T)$ of the HEA superconductors $(ZrNb)_{0.10}[MoReRu]_{0.90}$, $(HfTaWIr)_{0.40}[Re]_{0.60}$, and $(HfTaWPt)_{0.40}[Re]_{0.60}$ measured between 300 K and 1.7 K are shown in Fig. 6d–f. The normal-state resistivity data of all three materials reveals poor metallic behavior, with linear, only slightly decreasing $\rho(T)$ as a function of decreasing temperature. The room temperature (RT) resistivities are 105, 536, and 591 $\mu\Omega \text{cm}$, respectively, and very small residual resistivity ratio (RRR) values close to 1.00 are observed (compare Table S1, ESI[†]). The nearly temperature independent behavior of the resistivity and the high $\rho(\text{RT})$ values can be compared to the electron transport properties of strongly disordered alloys

and intermetallic compounds, as well as metallic glasses, where the scattering is caused by small domain size and atomic-scale disorder.

All three HEA superconductors $(ZrNb)_{0.10}[MoReRu]_{0.90}$, $(HfTaWIr)_{0.40}[Re]_{0.60}$, and $(HfTaWPt)_{0.40}[Re]_{0.60}$ reveal sharp transitions to the zero-resistance state according to their zero-field resistivity curves. The critical temperatures, *i.e.* $T_{c,\text{resistivity}}$, which were determined as the midpoints of the $\rho(T)$ plots, are consistent with the results from the magnetization and specific heat measurement (compare Table S1, ESI[†]). Only the $T_{c,\text{resistivity}}$ of $(ZrNb)_{0.10}[MoReRu]_{0.90}$ from the transport experiment is, at 5.74 K, slightly higher than the value estimated from the temperature dependent magnetization ($T_c \approx 5.3$ K). This common observation can be attributed to the higher sensitivity of the transport measurement to filamentary or surface superconductivity, which may appear at a slightly higher temperature than the bulk transition.

The upper critical fields $\mu_0 H_{c2}(T)$ were determined by applying the 50%-criterion to the resistivity data, *i.e.* T_c is taken as the

temperature where 50% of the normal-state resistivity is suppressed, measured from the field dependent $\rho(T)$ curves in the proximity of the superconducting transition (Fig. S4, ESI†). The temperature dependent critical fields $\mu_0 H_{c2}(T)$ of $(\text{ZrNb})_{0.10}[\text{MoReRu}]_{0.90}$, $(\text{HfTaWIr})_{0.40}[\text{Re}]_{0.60}$, and $(\text{HfTaWPt})_{0.40}[\text{Re}]_{0.60}$ are shown in Fig. S5 (ESI†). The approximation of the upper critical field at zero temperature $\mu_0 H_{c2}(0)$ of the three different α -Mn type HEA superconductors was performed by using the slopes dH_{c2}/dT of the linear region of $\mu_0 H_{c2}(T)$ for the Werthamer–Helfand–Hohenberg (WHH) expression in the dirty limit³⁴ according to the formula

$$\mu_0 H_{c2}(0) = -0.693 T_c \frac{d\mu_0 H_{c2}}{dT} \quad (1)$$

The obtained critical fields at zero temperature revealed relatively high zero temperature upper critical fields, of 7.86 T for $(\text{ZrNb})_{0.10}[\text{MoReRu}]_{0.90}$, 4.64 T for $(\text{HfTaWIr})_{0.40}[\text{Re}]_{0.60}$, and 5.90 T for $(\text{HfTaWPt})_{0.40}[\text{Re}]_{0.60}$.

Summary and conclusions

We have synthesized previously unreported High-Entropy Alloys in the pentanary systems $(\text{ZrNb})_{1-x}[\text{MoReRu}]_x$, $(\text{HfTaWIr})_{1-x}[\text{Re}]_x$, and $(\text{HfTaWPt})_{1-x}[\text{Re}]_x$ by arc-melting of the 4d- and 5d-transition metals. These new materials have body-centered cubic α -Mn-type structures and mixed site occupancies. Although the phase width for phase-pure samples is small for all three HEA series, the decrease of the lattice parameter a in samples with emerging impurity phases still indicates a systematic compositional change of the α -Mn type compounds. Whether the materials form a solid solution where all constituent elements mix randomly on all four crystallographic positions or if a certain ordering of the different metals on one or more symmetry site is existent cannot be determined unambiguously for a system with 5 elements of very similar electron count present and with conventional laboratory XRD data. The $(\text{ZrNb})_{1-x}[\text{MoReRu}]_x$, $(\text{HfTaWIr})_{1-x}[\text{Re}]_x$, and $(\text{HfTaWPt})_{1-x}[\text{Re}]_x$ HEAs are materials partway between ordered intermetallic compounds and random solid solutions stabilized within a small compositional range due to a delicate balance between the system's attempt to maximize the mixing entropy and minimizing the mixing enthalpy. The structure of these materials is quite a bit more complex than is found for the small-cell BCC superconducting HEAs, although the α -Mn structure type can be understood as a consequence of local closest packing, a straightforward structural principle. The presence of Re in significant proportion appears to be significant for the stabilization of the α -Mn-type although for the mixed 4d 5d system the Re is present at a much lower concentration than is typically found in binary alloys in this structure type, suggesting an entropic stabilization of this structure. The two purely 5d-metal based superconducting HEAs are the first of their kind.

Conflicts of interest

There are no conflicts to declare.

Acknowledgements

This work was supported by the Gordon and Betty Moore Foundation EPiQS program, grant GBMF-4412. The authors thank W. W. Xie for her insights into the α -Mn structure.

Notes and references

- Y. F. Ye, Q. Wang, J. Lu, C. T. Liu and Y. Yang, *Mater. Today*, 2016, **19**, 349.
- K. M. Youssef, A. J. Zaddach, C. Niu, D. L. Irving and C. C. Koch, *Mater. Res. Lett.*, 2015, **3**, 95.
- H. Kou, J. Lu and Y. Li, *Adv. Mater.*, 2014, **26**, 5518–5524.
- Y. Zou, H. Ma and R. Spolenak, *Nat. Commun.*, 2015, **6**, 7748.
- B. Gorr, M. Azim, H.-J. Christ, T. Mueller, D. Schliephake and M. Heilmayer, *J. Alloys Compd.*, 2015, **624**, 270.
- J.-W. Yeh, S.-K. Chen, S.-J. Lin, J.-Y. Gan, T.-S. Chin, T.-T. Shun, C.-H. Tsau and S.-Y. Chang, *Adv. Eng. Mater.*, 2004, **6**, 299.
- B. Cantor, I. T. H. Chang, P. Knight and A. J. B. Vincent, *Mater. Sci. Eng., A*, 2004, **375**, 213.
- C. L. Tracy, S. Park, D. R. Rittman, S. J. Zinkle, H. Bei, M. Lang, R. C. Ewing and W. L. Mao, *Nat. Commun.*, 2017, **8**, 15634.
- O. N. Senkov, J. D. Miller, D. B. Miracle and C. Woodward, *Nat. Commun.*, 2015, **6**, 6529.
- Y. Lu, Y. Dong, S. Guo, L. Jiang, H. Kang, T. Wang, B. Wen, Z. Wang, J. Jie and Z. Cao, *et al.*, *Sci. Rep.*, 2014, **4**, 6200.
- S. Guo, Q. Hu, C. Ng and C. T. Liu, *Intermetallics*, 2013, **41**, 96.
- P. Koželj, S. Vrnik, A. Jelen, S. Jazbec, Z. Jagličić, S. Maiti, M. Feuerbacher, W. Steurer and J. Dolinšek, *Phys. Rev. Lett.*, 2014, **113**, 107001.
- F. von Rohr, M. J. Winiarski, J. Tao, T. Klimczuk and R. J. Cava, *Proc. Natl. Acad. Sci. U. S. A.*, 2016, **113**, E7144.
- F. O. von Rohr and R. J. Cava, *Phys. Rev. Mater.*, 2018, **2**, 034801.
- J. Guo, H. Wang, F. von Rohr, Z. Wang, S. Cai, Y. Zhou, K. Yang, A. Li, S. Jiang and Q. Wu, *et al.*, *Proc. Natl. Acad. Sci. U. S. A.*, 2017, **114**, 13144.
- K. Stolze, J. Tao, F. O. von Rohr, T. Kong and R. J. Cava, *Chem. Mater.*, 2018, **30**, 906.
- S. Marik, M. Varghese, K. P. Sajilesh, D. Singh and R. P. Singh, *Cond. Mat.*, 2018, ArXiv180410092.
- J. A. Oberteuffer and J. A. Ibers, *Acta Crystallogr., Sect. B: Struct. Crystallogr. Cryst. Chem.*, 1970, **26**, 1499.
- W. Hornfeck, S. Thimmaiah, S. Lee and B. Harbrecht, *Chem. – Eur. J.*, 2004, **10**, 4616.
- B. T. Matthias, V. B. Compton and E. Corenzwit, *J. Phys. Chem. Solids*, 1961, **19**, 130.
- R. D. Blaughter and J. K. Hulm, *J. Phys. Chem. Solids*, 1961, **19**, 134; C. P. Poole and H. A. Farach, *J. Supercond.*, 2000, **13**, 47.
- B. J. Kim, H. Ohsumi, T. Komesu, S. Sakai, T. Morita, H. Takagi and T. Arima, *Science*, 2009, **323**, 1329–1332.

- 23 M. Ge, T. F. Qi, O. B. Korneta, D. E. De Long, P. Schlottmann, W. P. Crummett and G. Cao, *Phys. Rev. B: Condens. Matter Mater. Phys.*, 2011, **84**, 100402.
- 24 N. Haldolaarachchige, Q. Gibson, L. M. Schoop, H. Luo and R. J. Cava, *J. Phys.: Condens. Matter*, 2015, **27**, 185701.
- 25 TOPAS Software, Version 5, Bruker AXS Inc., 2014.
- 26 E. I. Gladyshevskii, M. A. Tylkina and E. M. Savitskii, *Kristallografiya*, 1960, **5**, 877.
- 27 E. Bucher, F. Heiniger and J. Mueller, *Helv. Phys. Acta*, 1961, **34**, 843–858.
- 28 B. T. Matthias, V. B. Compton and E. Corenzwit, *J. Phys. Chem. Solids*, 1961, **19**, 130.
- 29 J. Erlebacher, M. J. Aziz, A. Karma, N. Dimitrov and K. Sieradzki, *Nature*, 2001, **410**, 450.
- 30 I. McCue, E. Benn, B. Gaskey and J. Erlebacher, *Annu. Rev. Mater. Res.*, 2016, **46**, 263.
- 31 T. Song, M. Yan and M. Qian, *Corros. Sci.*, 2018, **134**, 78–98.
- 32 B. T. Matthias, *Phys. Rev.*, 1955, **97**, 74.
- 33 M. M. Collver and R. H. Hammond, *Phys. Rev. Lett.*, 1973, **30**, 92–95; M. M. Collver and R. H. Hammond, *Solid State Commun.*, 1977, **22**, 55.
- 34 N. R. Werthamer, E. Helfand and P. C. Hohenberg, *Phys. Rev.*, 1966, **147**, 295.